ChemComm

Check for updates

Tailored ultra-small Prussian blue-based nanoparticles for MRI imaging and combined photothermal/photoacoustic theranostics†

Lucile Fétiveau,[a] Gabriella Paul,[a] Alba Nicolas-Boluda,[b] Jeanne Volatron,[b] Riya George,[a] Sophie Laurent, [c] Robert Muller,[c] Lucie Sancey,[d] Philippe Mejanelle,[e] Alexandre Gloter,[f] Florence Gazeau [b] and Laure Catala ★[a]

Ultrasmall sub-10 nm nanoparticles of Prussian blue analogues incorporating Gd[III] ions at their periphery revealed longitudinal relaxivities above 40 mM^{-1} s^{-1} per Gd[III] regardless of the nature of the core and the polymer coating. Large T_1-weighted contrast enhancements were achieved in addition to a highly efficient photothermal effect and *in vivo* photoacoustic imaging in tumors.

Magnetic Resonance Imaging (MRI) is among the most powerful tools to perform diagnosis and staging because of its high resolution, deep tissue penetration and non-invasive character, despite its rather low sensitivity. Clinical T_1-contrast agents (CAs) based on Gd-chelates display longitudinal relaxivities r_1 on the order of 4 mM^{-1} s^{-1} and provide a positive contrast enhancement when the ratio r_2/r_1 remains below 2.[1–3] Release of free Gd^{3+} must be avoided because of its exchange with Ca^{2+} and its uptake by the brain when a patient is repeatedly exposed. In order to reduce these side-effects while maintaining a large contrast enhancement, new stable CAs with high relaxivities are required.[1] Strategies to slow down the rotation of the CAs have been reported by grafting Gd[III] chelates to polymers, proteins or nanoparticles.[4–7] Besides, the direct integration of the active Gd[III] ions into the scaffold of inorganic nanoparticles (NPs) has also been applied as a fruitful route to reduce the local motion of Gd[III] ions and lengthen efficiently

the rotational correlation time as well as increase their residence time. For non-porous NPs (oxides, phosphates,...), the Gd[III] ions located at their surface are active since coordinated water molecules undergo fast exchange with bulk water while most of the Gd[III] ions embedded within the particle's core are less active (no water exchange) but may still increase the risks related to Gd[III] injection.[8–10] Besides, nanoparticles of microporous compounds, to which Prussian blue analogues (PBA) belong, have emerged as appealing nano-platforms for biomedical applications.[11–13]

One main advantage of PBA NPs is that the proportion of atoms located at their surface is much larger than that of non-porous nanomaterials while having a much larger stability under diluted conditions than other Metal Organic Frameworks (MOFs). A 3 nm PBA particle has 64% of its atoms located at its surface, almost twice that of an iron NP of the same size. Few examples of pure gadolinium hexacyanoferrate NPs were reported with r_1 ranging from 13 to 38 mM^{-1} s^{-1}/Gd[III] for inorganic cores of sizes around 3 to 25 nm particles, sometimes aggregated.[14–16]

In this work, we targeted ultra-small nanoparticles PBA cores with Gd[III] mainly located at their periphery to achieve large relaxivities and reduce the local Gd[III] concentration needed to perform MRI diagnosis. The importance of localization of the active ions in PBA NPs was first reported on Mn[II]InFe NPs by our group.[17] Later on, Gd[III]-containing PB nanocrystals of 60 nm to 110 nm or 360 nm hollow PB revealed r_1 = 12 mM^{-1} s^{-1} (at 1.4 T) to 39 mM^{-1} s^{-1} (at 3 T)/Gd[III] neglecting the contribution of Fe[III].[18–20] These values are moderate for such large sizes due to core-embedded Gd[III] atoms.

Here we report outstanding longitudinal relaxivities of 40 mM^{-1} s^{-1} per Gd[III] found for two series of ultrasmall NPs containing either a diamagnetic core (In[III][Fe[II](CN)$_6$]) or a paramagnetic one (Prussian blue Fe[III][Fe[II](CN)$_6$]) with different Gd[III] contents, accompanied by the high photothermal effect of the PB-based NPs. Importantly, these nanoparticles were prepared by a green process at room temperature. The strong insolubility of the selected PBA was a key point to favor the

[a] *Institut de Chimie Moléculaire et des Matériaux d'Orsay, CNRS, Université Paris Sud Paris Saclay, 91405 Orsay, France. E-mail: laure.catala@u-psud.fr*

[b] *Laboratoire MSC, Université de Paris, CNRS, 12 rue Alice Domon et Léonie Duquet, 75013 Paris, France*

[c] *Univ. Mons., NMR & Mol Imaging Lab., Dept. Gen. Organ. & Biomed. Chem., B-7000 Mons, Belgium*

[d] *Institute for Advanced Biosciences, INSERM U1209, CNRS UMR 5309, Université Grenoble Alpes, 38000 Grenoble, France*

[e] *IUT Orsay, Université Paris Sud Paris Saclay, 91405 Orsay, France*

[f] *Laboratoire de Physique des Solides, Université Paris Sud Paris Saclay, 91405 Orsay, France*

† Electronic supplementary information (ESI) available: Experimental details, XRPD, IR spectra, MRI phantoms, and photoacoustic images. See DOI: 10.1039/c9cc07116d

formation of core–shell like structures with Gd^{III} atoms at the periphery in a one-pot process without any additive. The positive role of the PB core was highlighted as both remarkable T_1 contrast enhancement and efficient photothermal therapy (PTT) at low concentrations. Despite the small size of the PB core, their PTT efficiency exceeded those of other PTT agents and was monitored *in vivo* by photoacoustic imaging.

The synthesis consisted in a fast mixture at 2 °C of aqueous solutions of hexacyanoferrate (0.5 mM) and an aqueous solution containing x% of Gd^{III} and $1 - x$% of Y = In^{III} or Fe^{III} (with $[Gd^{III} + Y] = 0.5$ mM). Compositions were scanned in a range of $x = [Gd^{III}]/[Gd^{III} + Y^{III}] = 0.05$ to 0.8. The immediate change of the colloidal solution to blue was observed in the case of Y = Fe^{III} due to the metal-to-metal charge transfer (MMCT) of PB,[21] while no color change occurred as expected with Y = In^{III}. The colloidal solutions remained stable during several weeks for $x < 0.5$, with a negative ζ potential of around -30 mV due to the presence of hexacyanoferrate coordinated at the surface. Addition of dextran (25 equivalents of monomer with respect to Y) and acetone led to the recovery of powders of NPs after centrifugation. X-ray powder diffraction (XRPD) showed only the reflection peaks of the face centered cubic structure (fcc) of PBA discarding any trace of segregation for the lower Gd^{III} content ($x < 0.1$). Above $x \geq 0.15$, a few larger NPs of $KGd^{III}[Fe^{II}(CN)_6] \cdot H_2O$ were detected in the XRPD pattern and by Transmission Electron Microscopy (TEM) imaging (for $x > 0.15$ Fig. S1 and S2, ESI†). This phase segregation was not surprising since $KGd^{III}[Fe^{II}(CN)_6] \cdot H_2O$ has an orthorhombic structure[14] that impedes epitaxial growth on the fcc structure of the PBA cores. We focused therefore on the lowest Gd^{III} contents ($x = 0.05$ and 0.1) denoted in the following as GdYFe[5] or GdYFe[10] (Y = In^{III} or Fe^{III}). High crystallinity of the cores was achieved for the four samples as correlation lengths of 5 nm were extracted from the XRPD patterns (Fig. S3, ESI†).

Importantly, the powders of NPs coated with dextran were dispersed back in water without aggregation (as shown by DLS in Fig. S4, ESI†) and their ζ potentials remained slightly negative, around -15 mV (Fig. S5, ESI†). TEM confirmed the presence of homogeneous and non-aggregated nanoparticles with similar average sizes between 3 and 4 nm (Fig. 1a and Fig. S1, ESI†). Importantly, STEM-EELS micro-spectroscopy performed on an assembly of GdInFe[5]@NPs allowed detecting (despite the weak concentration of metallic atoms for such NPs) the concomitant presence of Gd, In and Fe in each NP (Fig. 1b, c and Fig. S7, S8 with detailed explanation, ESI†). This ruled out any phase separation as only a few percent of pure KGdFe would be detected. The chemical compositions were determined by ICP and elemental analysis. Metallic and dextran contents were in good agreement with those introduced initially (Fig. S9, ESI†).‡ Fourier Transform Infra-Red (FTIR) spectroscopy was carried out on the four samples in the $200–4000$ cm^{-1} range (Fig. S10, ESI†). In both GdInFe samples, asymmetric vibrations of cyanide bridges were detected at 2108 cm^{-1} and 2076 cm^{-1} and were assigned to the In^{III}-NC-Fe^{II} and Gd^{III}-NC-Fe^{II} pairs respectively.[14] In the case of both GdFeFe samples, cyanide vibrations for Fe^{III}-NC-Fe^{II} and Gd^{III}-NC-Fe^{II} pairs
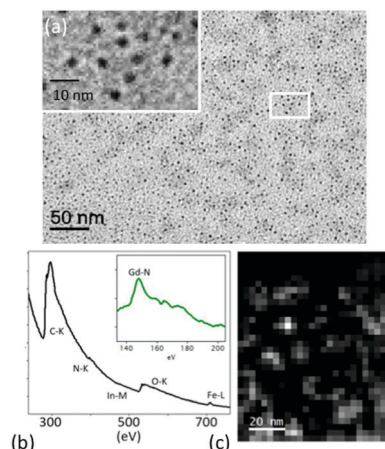

Fig. 1 (a) TEM micrograph of GdInFe[5]@dextran NPs; (b) EELS spectral component of GdInFe[5]@dextran with C, N, In and Fe edges and zoom on Gd edges; (c) EELS map where bright areas correspond to the spectral component demonstrating the localisation of C, N, In, Fe and Gd in the NPs.

are much closer in energy (2070 cm^{-1} and 2076 cm^{-1} respectively) and are thus difficult to discriminate, even though a broadening suggests the presence of both contributions (Fig. S9b, ESI†). The low frequency region further supports the coordination of Gd^{III} to the PBA cores as two contributions are observed for all particles compared to the pure PBA counterparts (Fig. S9, ESI†), as also reported on larger hollow structures.[20] FTIR, XRPD and STEM-EELS data are consistent with the presence of Gd^{III}-NC-Fe^{II} pairs at the surface of the PBA cores, as shown also for $MnIn[Fe^{II}(CN)_6]$ NPs.[13]

In order to compare the relaxivities of the four samples GdYFe[5] and GdYFe[10] (Y = In^{III} or Fe^{III}), nuclear magnetic relaxation dispersion (NMRD) profiles were recorded at 37 °C on aqueous dispersions (Fig. 2). The frequency dependence of the longitudinal relaxivity r_1 displays the characteristic shape of slow tumbling species, with a maximum at 60 MHz (1.4 T).[1] Exceptional longitudinal relaxivities were reproduced on several batches for the four types of NPs with values of $r_1 \geq 40$ mM^{-1} s^{-1}.
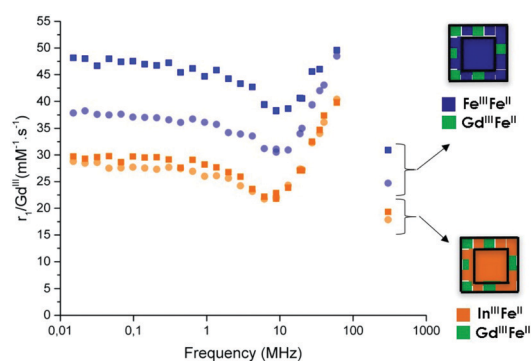

Fig. 2 NMRD profiles showing r_1 per mM of Gd^{III} with respect to the Larmor frequency obtained at 37 °C plotted in blue for Y = Fe^{III} (squares for $x = 0.05$ and circles for $x = 0.1$) and in orange for Y = In^{III} (squares for $x = 0.05$ and circles for $x = 0.1$); schematic view of the NPs with GdFe pairs in green on either InFe core (orange) or FeFe core (blue).

Table 1 Longitudinal relaxivities obtained per mM of Gd^{III} at 37 °C and 5 °C at 1.4 T, and r_2/r_1 values at 37 °C

	GdInFe[5]	GdInFe[10]	GdFeFe[5]	GdFeFe[10]
Size (nm)	3.6 ± 0.7	3.6 ± 0.8	3.9 ± 1.0	3.4 ± 0.6
r_1, mM^{-1} s^{-1} (37 °C)	40	40	55	46
r_1, mM^{-1} s^{-1} (5 °C)	62	62	81	70
r_2/r_1 (37 °C)	1.3	1.4	1.4	1.5

Fig. 3 T_1-Weighted MR images recorded under a field of 7 T at 37 °C with a spin-echo sequence (TR = 22 ms and TE = 3 ms) at $[Gd^{III}]$ = 0.2 mM for, from left to right: water, GdFeFe[5], GdFeFe[10], GdInFe[5] GdInFe[10] all coated with dextran, and Gd-DTPA (Prohance).

Moreover, relaxivities increased when lowering the temperature to 5 °C (Table 1) due to the increase of the rotational correlation time. This suggests that the longitudinal relaxivity is limited by the slow tumbling rather than by the water residence time for the four samples. Their efficiency as T_1-contrast agents was confirmed as a r_2/r_1 ratio below 2 was obtained.

The constant value of r_1 = 40 mM^{-1} s^{-1} per Gd^{III} obtained for GdInFe[5] and GdInFe[10] shows that magnetic dipolar interactions among Gd^{III} ions can be neglected for such low Gd^{III} concentrations. However, for GdFeFe NPs, in addition to Gd^{III} ions, paramagnetic Fe^{III} ions are also located at the surface and contribute to some extent to the overall relaxivity. This has always been neglected in the literature on PB NPs doped with Gd^{III} or Mn^{II}.

To estimate the contribution of Fe^{III} ions only, the longitudinal relaxivity value of a reference sample of 4 nm pure PB@dextran NPs was estimated and was found to be r_1 = 1.2 mM^{-1} s^{-1} per Fe^{III} ion located at the surface. Despite this moderate value, the large proportion of Fe^{III} ions at the surface of GdFeFe[5] and GdFeFe[10] NPs (94% and 89% respectively of total surface atoms, detailed calculations are provided in the ESI†) leads to an estimated contribution of Fe^{III} to a relaxivity of 19% for GdFeFe[5] and 10% for GdFeFe[10] to the total NP's relaxivity. This means that there is good agreement between the four samples, with a constant value of r_1 = 40 mM^{-1} s^{-1} (at 1.4 T) per Gd^{III} ion and additional contribution of Fe^{III} in the case of GdFeFe samples that induces the overestimated "apparent" values (46 and 55 mM^{-1} s^{-1}) reported in Table 1.

Moreover, by changing the nature of the coating from dextran to polyvinylpyrrolidone (PVP) while maintaining the core exactly the same for GdFeFe[5] and GdInFe[5], NMRD profiles were found to be similar and resulted in close relaxivity values thus confirming that the coating may be modified while maintaining a similar efficiency (Fig. S12, ESI†). These unprecedented values for sub-10 nm NPs are attributed to the location of Gd^{III} ions at their surface. They are three to four times more efficient than 3 nm $KGd^{III}[Fe^{II}(CN)_6]\cdot H_2O$ and 60 nm PB particles doped with 15% Gd^{III},[16,18] four times that of Gd_2O_3 nanoparticles of the same size,[12] and ten times that of clinical CAs.

Interestingly, this strongly reduces the dose of Gd^{III} needed to perform MRI imaging. T_1-Weighted contrasts were recorded at 37 °C at low concentrations ($[Gd^{III}]$ = 0.2 mM) on all samples coated with dextran under a high field of 7 T. T_1-Contrast enhancement at this field is generally much weaker for paramagnetic nanoparticles than for conventional CAs. Still, all the four samples provided a much brighter contrast enhancement than a 0.2 mM Gd-DTPA (Prohance) solution (Fig. 3 and Fig. S11, ESI†). The best T_1-weighted contrast enhancement

was observed for GdFeFe[5] NPs as compared to the other samples. It remained important even for $[Gd^{III}]$ = 0.05 mM (Fig. S12, ESI†). Importantly, the Gd^{III} content was analyzed after ultrafiltration of diluted colloidal solutions of the NPs (0.1 mM in Gd^{III}) and showed negligible leaching of the Gd^{III} ions (Fig. S10, ESI†): 0.16 ppm for GdFeFe particles (less than 10%) and below 0.03 ppm for GdInFe particles (less than 2%).§ Toxicity studies on human glioma U87-MG cells showed good viability after 24 h of incubation confirming the low toxicity reported in the literature for related systems on several other cell types (Fig. S14, ESI†).[14,17–20]

Besides MRI diagnosis, PB-based NPs are highly appealing as PB may be active in photothermal therapy (PTT) due to its intense intervalence band in the 600–800 nm range. Indeed, a temperature increase of almost 25 °C (with a local temperature of 50 °C) was achieved when irradiating an aqueous dispersion of GdFeFe[5] containing 45 μg mL^{-1} of PB (Fig. 4a) with an 808 nm laser at a power of 1 W cm^{-2}. Lower concentrations of GdFeFe NPs may be used to adjust temperatures around 42 °C as shown in the ESI† (Fig. S15). This photothermal effect was slightly larger than that obtained for 50 μg mL^{-1} of Au using commercial gold nanorods and 50 μg mL^{-1} of 400 nm carbon
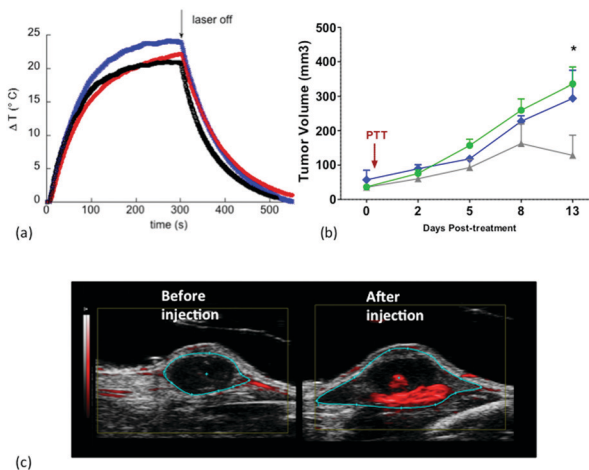
Fig. 4 (a) Photothermal effect of an aqueous dispersion of 45 μg mL^{-1} of GdFeFe[5] (blue), 50 μg mL^{-1} of gold nanorods (red) and 50 μg mL^{-1} of MWNTs (black) under laser irradiation (808 nm, 1 W cm^{-2}) for 300 s. (b) Tumor growth evolution of CT26 colon tumor xenograft injected with 25 μg of GdFeFe[5]@(dextran)$_{25}$ and irradiated with an 808 nm laser (grey) compared to the laser only group (blue) and control group (green). (c) Photoacoustic image of the tumor before and after intratumoral injection of 25 μg of GdFeFe[5] irradiation at 808 nm, the photoacoustic signal (>0.6 a.u.) due to NPs is shown in red.

nanotubes measured exactly under the same conditions (Fig. 4a), indicating the high efficiency of our ultrasmall PB-based NPs in colloidal suspension. To further demonstrate that PTT was efficient *in vivo*, an intratumoral injection of 25 µg of GdFeFe[5] was performed in a subcutaneous model of murine colon carcinoma (CT26) followed by irradiation with an 808 nm laser for 180 s. The surface temperature of the tumor was monitored using an infrared camera. The temperature rose up to 50 °C in the central part of the tumor (Fig. 4c and Fig. S13, ESI†). A significant reduction of tumor growth was observed in tumors that had undergone GdFeFe[5]-mediated PTT compared to the control tumor experiments (with laser only or without any treatment, Fig. 4b). In addition, to determine the potential of GdFeFe[5] as a multimodal contrast agent, photoacoustic imaging (PAI) of the tumor was performed before and after GdFeFe[5] injection. A clear photo-acoustic signal (~ 808 nm) was observed intratumorally (Fig. 4c) and was still persistent after irradiation (Fig. S14, ESI†).

In a nutshell, the design of ultrasmall PBA-based nanoparticles with a surface enriched with Gd^{III} is a successful route to reach optimal longitudinal relaxivities of around 40 mM^{-1} s^{-1} per Gd^{III} ion, larger than that of any other NP (below 100 nm). The local concentration required for T_1 contrast enhancement is thus highly reduced even at high field. Importantly, they are obtained by a room-temperature, stabilizer-free one-pot green process. Interestingly, the respective contributions of paramagnetic Fe^{III} and Gd^{III} ions were accurately determined by a comparative study of the four samples. PB-based particles appeared as the most promising candidates for theranostics. In addition to the very high relaxivity values obtained compared to Prohance that reduces the amount of Gd^{3+} by a factor of 10, these nanoparticles have a PTT efficiency that overcomes those of gold nanostructures and carbon nanotubes. They remained efficient for PAI *in vivo* after intra-tumoral injection. Furthermore, they may have longer retention times. As a next step, biodistribution after intravenous injection will be monitored by *in vivo* MRI to determine the fate of these new ultrasmall NPs. Theranostic NPs that can undergo renal excretion when accumulated by the Enhanced Permeation Retention effect are highly appealing as reported.[22–24] This goal has to be addressed in the case of PB-based NPs. Our one-step green costless synthesis with tunable composition for both the sub-5 nm inorganic core and the coating is a versatile route to reach this goal and achieve optimised theranostics in a close future.

Conflicts of interest

There are no conflicts to declare.

Notes and references

‡ The content in dextran is chosen to achieve full dispersion after drying without aggregation while providing optimal relaxivities.

§ A process based on xylenol assay confirmed the low leaching in foetal bovine serum (Fig. S10 and explanations in the ESI†).

1 É. Tóth, L. Helm and A. E. Merbach, *Top. Curr. Chem.*, 2002, **221**, 61–101.
2 J. Wahsner, E. M. Gale, A. Rodríguez-Rodríguez and P. Caravan, *Chem. Rev.*, 2019, **119**, 957–1057.
3 L. Helm, *Prog. Nucl. Magn. Reson. Spectrosc.*, 2006, **49**, 45–64.
4 K. Nwe, D. Milenic, L. H. Bryant, C. A. S. Regino and M. W. Brechbiel, *J. Inorg. Biochem.*, 2011, **105**, 722–727.
5 S. Liu, P. Zhang, S. R. Banerjee, J. Xu, M. G. Pomper and H. Cui, *Nanoscale*, 2015, **7**, 9462–9466.
6 A. Mignot, C. Truillet, F. Lux, L. Sancey, C. Louis, F. Denat, F. Boschetti, L. Bocher, A. Gloter, O. Stéohan, R. Antoine, P. Dugourd, D. Luneau, G. Novitchi, L. C. Figueiredo, P. Cesar de Morais, L. Bonneviot, B. Albela, F. Ribot, L. Van Lokeren, I. Déchanmps-Olivier, C. Françoise, G. Lemercier, C. Villiers, P. N. Marche, S. Le Duc, S. Roux, O. Tillement and P. Perriat, *Chem. – Eur. J.*, 2013, **19**, 6122–6136.
7 F. Lux, A. Mignot, P. Mowat, C. Louis, S. Dufort, C. Bernhard, F. Denat, F. Boschetti, C. Brunet, R. Antoine, P. Dugourd, S. Laurent, L. V. Elst, R. Muller, L. Sancey, V. Josserand, J. L. Coll, V. Stupar, E. Barbier, C. Rémy, A. Broisat, C. Ghezzi, G. Le Duc, S. Roux, P. Perriat and O. Tillement, *Angew. Chem., Int. Ed.*, 2011, **50**, 12299–12303.
8 H. Dong, S.-R. Du, X.-Y. Zheng, G.-M. Lyu, L.-D. Sun, L.-D. Li, P.-Z. Zhang, C. Zhang and C.-H. Yan, *Chem. Rev.*, 2015, **115**, 10725–10815.
9 J. L. Bridot, A. C. Faure, S. Laurent, C. Rivière, C. Billotey, B. Hiba, M. Janier, V. Josserand, J. L. Coll, L. Vander Elst, R. Muller, S. Roux, P. Perriat and O. Tillement, *J. Am. Chem. Soc.*, 2007, **129**, 5076–5084.
10 H. Hifumi, S. Yamaoka, A. Tanimoto, D. Citterio and K. Suzuki, *J. Am. Chem. Soc.*, 2006, 2–7.
11 P. Horcajada, R. Gref, T. Baati, P. K. Allan, G. Maurin, P. Couvreur, G. Férey, R. E. Morris and C. Serre, *Chem. Rev.*, 2012, **112**, 1232–1268.
12 L. Catala and T. Mallah, *Coord. Chem. Rev.*, 2017, **346**, 32–61.
13 J. Long, Y. Guari, C. Guérin and J. Larionova, *Dalton Trans.*, 2016, **45**, 17581–17587.
14 V. S. Perera, L. D. Yang, J. Hao, G. Chen, B. O. Erokwu, C. A. Flask, P. Y. Zavalij, J. P. Basilion and S. D. Huang, *Langmuir*, 2014, **30**, 12018–12026.
15 Y. Guari, J. Larionova, M. Corti, A. Lascialfari, M. Marinone, G. Poletti, K. Molvinger and C. Guérin, *Dalton Trans.*, 2008, 3658–3660.
16 M. Perrier, S. Kenouche, J. Long, K. Thangavel, J. Larionova, C. Goze-Bac, A. Lascialfari, M. Mariani, N. Baril, C. Guérin, B. Donnadieu, A. Trifonov and Y. Guari, *Inorg. Chem.*, 2013, **52**, 13402–13414.
17 G. Paul, Y. Prado, N. Dia, E. Rivière, S. Laurent, M. Roch, L. Vander Elst, R. N. Muller, L. Sancey, P. Perriat, O. Tillement, T. Mallah and L. Catala, *Chem. Commun.*, 2014, **50**, 6740–6743.
18 Y. Li, C. H. Li and D. R. Talham, *Nanoscale*, 2015, **7**, 5209–5216.
19 M. F. Dumont, H. a. Hoffman, P. R. S. Yoon, L. S. Conklin, S. R. Saha, J. Paglione, R. W. Sze and R. Fernandes, *Bioconjugate Chem.*, 2014, **25**, 129–137.
20 X. Cai, W. Gao, L. Zhang, M. Ma, T. Liu, W. Du, Y. Zheng, H. Chen and J. Shi, *ACS Nano*, 2016, **10**, 11115–11126.
21 K. Itaya and I. Uchida, *Inorg. Chem.*, 1986, **25**, 389–392.
22 S. Kotb, A. Detappe, F. Lux, F. Appaix, E. L. Barbier, V.-L. Tran, M. Plissonneau, H. Gehan, F. Lefranc, C. Rodriguez-Lafrasse, C. Verry, R. Berbeco, O. Tillement and L. Sancey, *Theranostics*, 2016, **6**, 418–427.
23 L. Sancey, S. Kotb, C. Trulllet, F. Appaix, A. Marais, E. Thomas, B. van der Sanden, J.-P. Klein, B. Laurent, M. Cottier, R. Antoine, P. Dugourd, G. Panczer, F. Lux, P. Perriat, V. Motto-Ros and O. Tillement, *ACS Nano*, 2015, **9**, 2477–2488.
24 F. Liu, X. He, H. Chen, J. Zhang, H. Zhang and Z. Wang, *Nat. Commun.*, 2015, **6**, 8003.